PROCEEDINGS, 50th Workshop on Geothermal Reservoir Engineering
Stanford University, Stanford, California, February 10-12, 2025
SGP-TR-229

Redistributed Seismicity at the Coso Geothermal Field Investigated Through Stress Changes from Fluid Production and Migration

Sui Tung, Manoochehr Shirzaei, Timothy Masterlark, Herbert Wang, Wei-Chuang Huang, Kurt Feig

Science Building, 1200, 125 Memorial Circle, Lubbock, TX 79409

Jay.sui.tung@ttu.edu

Keywords: Coso, poroelastic, thermoelastic, stress triggering, finite element, InSAR, reduced seismicity

ABSTRACT

The Coso geothermal field of southern California hosts one of the major geothermal power plants and was launched with energy production in 1986. Through looking at the relocated seismicity data from SCEC, we observed that low-magnitude seismic events (magnitude < 4) are unevenly distributed across three distinct zones: the nearfield (less than 3 km), midfield (3-6 km), and far-field (greater than 6 km) from the Coso geothermal plant. These zones demonstrate noticeable changes in earthquake locations before and during geothermal production. Since the production was launched, the midfield region of the main flank has shown a significant drop in seismicity rate compared to surrounding areas before production. Between 1986 and 2019, far-field earthquakes clustered in the eastern and western parts of the greater Coso area, while pre-production events during 1981-1986 were more evenly distributed along the NW-SE and SW-NW trending structures within the geothermal field. InSAR time series data reveal surface subsidence (rate up to 14 mm/year) over the field since 2014, which is then reconciled with finite-element-based poroelastic simulations. The simulations estimate stress evolution and illustrate how the spatiotemporal distribution of seismicity is linked to stress changes perturbed by fluid migration during geothermal operations. Before the 2019 Ridgecrest earthquake (2014-2019), approximately 70% of co-production earthquake events from 2014 to 2019 occurs in zones of increased Coulomb stress with greater than 99% confidence. Meanwhile, the midfield zone, characterized by reduced seismicity, coincides with a region of decreasing pore-fluid pressure. This is also consistent with aftershock distributions and surface subsidence (rate up to 10 mm/year) that are continuously observed after the Ridgecrest earthquake. These findings provide a physical explanation for how decades of geothermal operations at Coso have altered the stress field and contributed to the evolving seismic patterns, offering valuable insights for assessing seismic hazards in other geothermal regions.

1. INTRODUCTION

The Coso area in Southern California, the third-largest geothermal field in the U.S., has produced up to 270 MWe of electricity for nearly four decades. With net fluid production of around 1.3 x 10^9 kg per month (Figure 1), it hosts high-temperature geothermal reservoirs where thermal destressing prohibits seismicity (Im et al., 2021) and micro-seismic events might be triggered by regional tectonic loading and remote earthquakes (Hauksson and Unruh, 2007; Zhang et al., 2017). This study analyzes seismicity near Coso since 1981, examining how distribution patterns have changed before and during industrial energy production operations. We identify seismic zoning patterns, identify potential anthropogenic earthquake triggering, and use numerical simulations to model fluid-crust interactions. Comparing model predictions with spatiotemporal seismicity changes and surface displacement rates obtained from satellite radar images, we investigate if Coulomb stress changes perturbed by energy production facilitate seismic zoning.

2. SEISMICITY REDISTRIBUTION BEFORE AND DURING GEOTHERMAL ENERGY PRODUCTION

Based on the relocated earthquake catalog (between 2014 and 2019) provided by the Southern California Seismic Network (SCSN) (Hauksson et al., 2020), three distinct seismic zones are identified within the Coso area according to the spatiotemporal distribution of seismicity rate during 1981-2019, measured as the number of events per year per km² (Figure 2 and Figure 3). Zone 1, located within 3 km of the main production flank, is termed the "nearfield"; Zone 2, the elliptical area in Figure 3, is called the "midfield" (3 - 6 km from the production flank); and Zone 3 is the "farfield" (> 6 km from the production flank (Figure 3). These seismic zones, which do not overlap, occurred after power production launched in May 1986 (CDC, 2022) (Figure 2). Zone 1 covers most of the geothermal wells (Figure 2), where the seismicity is very shallow there (depth < 4 km) and associated with a shallow low-velocity heat source (Davatzes and Hickman, 2010). These shallow events are likely related to geothermal operations (Schoenball et al., 2015; Zhang and Lin, 2014), as being very close (< 1 km) to the wellbore locations (Figure 2 and Figure 3b) (Kaven et al., 2011). Such proximity between seismicity and wellbores has also been observed at other geothermal power plants (e.g., Bachmann et al., 2012; Cardiff et al., 2018; Ellsworth et al., 2019; Feigl et al., 2022; Juncu et al., 2020; Li et al., 2021; Yeo et al., 2020). Similarly, Zone 3 showed a 50% increase in seismicity rate during the production period compared to the pre-production period (Figure 2 and Figure 3). On the contrary, Zone 2 experienced significantly fewer seismic events (Figure 2 and Figure 3) after geothermal production began in 1986. Its seismicity rate decreased by ~90% from ~70 events per year during the pre-production period (1981-1986) to <10 events per year during the co-production period (2014-2019) (Figure 2 and Figure 3). Within 6 months after the 2019 July 4 Ridgecrest earthquakes (RE), the aftershocks were located along the NW-SE trending fashion propagating from the RE epicenter but appeared to “jump” over the Coso field and reappeared in the Owen Valley fault zone (Figure 2). This is a very intriguing phenomenon that might be related to the thermal distressing process at the Coso geothermal field (Im et al., 2021). The aftershock activity slowly retreated from the geothermal field (Figure 2e), with clustering at the Owen Valley fault zone to the north and Ridgecrest faults to the south. While our previous work focuses on the pre-Ridgecrest seismic

sequence (Tung et al., 2024), our current plan is to extend the study to investigate how the Ridgecrest aftershock pattern over the Coso field could be relevant to the energy production activities there.

3. POROELASTIC SIMULATION OF FLUID-ROCK COUPLING

Poroelastic finite element models (FEMs) are built to simulate the hydromechanical coupling between the pore-fluid migration and rock deformation during geothermal production (Figure 4). Such simulation is initialized by the fluid production and injection rates reported monthly by the Department of Conservation, California (https://www.conservation.ca.gov) since 1986. The mean production and injection rates are respectively 3.2×10^7 and 1.6×10^7 m^3/year, giving rise to the mean net production of 1.6×10^7 m^3/year, assuming the pore liquid water medium. The spatiotemporal evolution of surface displacement (Figure 5), and Coulomb stress change (Figure 5) are simulated, as the crustal medium is driven by pore-fluid migration (Figure 4e) since the energy production began. The modeling domain hosts a non-uniform distribution of poroelastic materials (Table 1) (c.f. Im et al., 2021; Tung and Masterlark, 2018; Tung et al., 2018; Tung et al., 2021), as compared to other analytical solutions assuming layered geological structures (Barbour et al., 2016; Barbour et al., 2017; Eneva et al., 2018; Goebel et al., 2017; Goebel and Brodsky, 2018; Li et al., 2021; Tung et al., 2021). The elastic moduli (Figure 4a and Figure 4b) are compiled from the SCEC community seismic velocity model (Plesch et al., 2011) and CRUST2.0 (Bassin et al., 2000), while the poroelastic parameters including the intrinsic rock permeability k and porosity φ are described by a simplified geological model (Figure 3f and Table 1).

4. SURFACE SUBSIDENCE OVER THE COSO PRODUCTION FLANKS

We employed Interferometric Synthetic Aperture Radar (InSAR) data from the Sentinel-1A/B satellites, following ascending path 64 (dA64) and descending path 71 (dD71) (Figure 5), to map the surface displacement rate across the greater Coso area. The Sentinel-1 data was processed using GAMMA (Werner et al., 2000) and PYGMTSAR. Atmospheric delay correction and time-series extraction were implemented using an array of filters (Lee and Shirzaei, 2023; Shirzaei et al., 2013) to separate deformation signals from nuisance effects such as orbital, topographic, and atmospheric disturbances. Cross-correlation analysis was then applied to identify and down-weight the effect of atmospheric delay (Shirzaei and Bürgmann, 2012). The interferograms captured ground displacement history in two periods during geothermal production namely, (1) 2014 to 2019 (Figure 5) and (2) 2020 – 2022 (Figure 6 and Figure 7). Up to 14 mm/year and 10mm/year of subsidence are mapped respectively in periods (1) and (2) along the satellite line-of-sight (LOS) direction. For the period (1), we use the poroelastic model and thermal cooling model to recover the subsidence amplitude (Figure 5g and Figure 5h). Future work will be conducted the similar analysis in the period (1).

5. TRANSIENT STRESS TRIGGERING/SHADOWING AND SEISMIC DISTRIBUTION

Based on the 3D stress tensor evolution and 100 poroelastic scenarios simulated by the poroelastic model, we calculate the Coulomb stress changes over the greater Coso area from 1986 – to 2021. We then compare the results to the seismicity patterns observed during the production activities (Figure 8). Generally, the spatial patterns of ΔCFS and co-production seismic density both exhibit a similar "butterfly" pattern (Figure 3 and Figure 8). Approximately 70% of seismic locations (Figure 3a) experience $\Delta CFS \geq 0$ during production, while only 33% of pre-production seismic locations (Figure 3b) fall within the zone of $\Delta CFS \geq 0$ (Figure 8). Those seismic events of the former attain a mean ΔCFS of 14 kPa and a maximum of 35 kPa per year, exceeding the commonly accepted triggering threshold of 10 kPa (King et al., 1994; Stein, 1999; Yeo et al., 2020). Notably, the Coso area experienced fewer seismic events within Zone 2 after 1986, as do the northern and southern parts of Zone 3 (Figure 3b). These regions fall into the zone of $\Delta CFS < 0$ (Figure 8) calculated using the poroelastic model. In contrast, areas of positive ΔCFS rates overlap well with the two lobes of relatively high seismic density east and west of the Coso field since 1986 (Figure 8). This suggests that power production activities might have maintained or even enhanced the seismic activity east and west of the Coso area along the Coso Range and Rose Valley within Zone 3 (Figure 8).

6. DISCUSSION & CONCLUSIONS

As detailed above, Zone 2 and the northern and southern parts of Zone 3 have seen a notable decrease in seismic activity since the onset of production (Figure 3b), even though these areas were seismically active before the production period (Figure 3a). The overlap of negative seismicity rate and stress change indicates that reduced Coulomb stress stabilizes faults in the northern and southern parts of Zone 3 (Figure 8). Local positive anomalies ΔCFS explain the increased seismicity rate near the geothermal wells in Zone 1 (Figure 8).

However, the seismic paucity within Zone 2 appears to correlate with the pore pressure components (Tung et al., 2024). Instead, diminished seismic activity in Zone 2 consistently aligns with negative ΔP (up to 20 MPa) accumulated within the reservoir boundary since 1986 (Figure 4 and Figure 8). The western reservoir boundary (Figure 4f) and its hydrological disconnection from the Coso field are supported by asynchronous pressure variations over time with the main flank (Sabin et al., 2016; Siler et al., 2016). Interestingly, the modeled east-west extent of negative ΔP and thus ΔCFS is bounded by the lateral boundary of the permeable reservoir (Figure 8), aligning with the observed low seismicity rate in Zone 2 (Figure 1b). Figure 8 shows that Zone 2's seismic paucity is associated with a large negative ΔCFS (~25 MPa) accumulated since 1986 due to pore-fluid migration. Our simulation results indicate that pore-fluid migration is a viable mechanism for clamping/stabilizing faults within Zone 2.

To sum up, faults at varying distances from the geothermal reservoir (Zones 1, 2, and 3) experience different degrees of stress triggering, interacting with the reservoir's permeability structure. Our study suggests that long-term geothermal production at Coso has influenced nearby fault stability and contributed to the spatiotemporal distribution of seismic zoning. This provides valuable insights for assessing seismic hazards in other geothermal areas. Physics-based models and a deeper understanding of reservoir geological/permeability structures will further enhance the hazard assessment accuracy and potentially inform strategies for reducing seismic risk during geothermal energy exploitation.

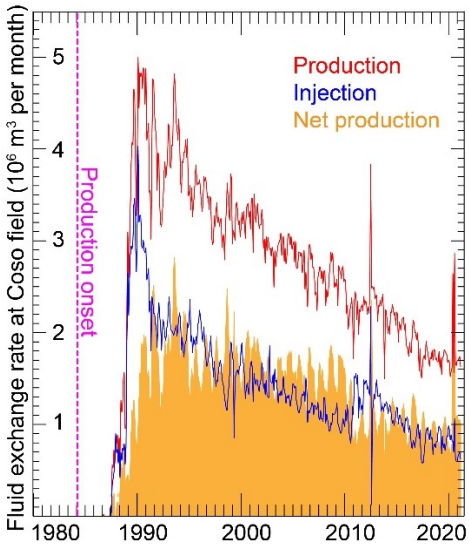

Figure 1. Historical rate of production injection and net production at the Coso geothermal power plant.

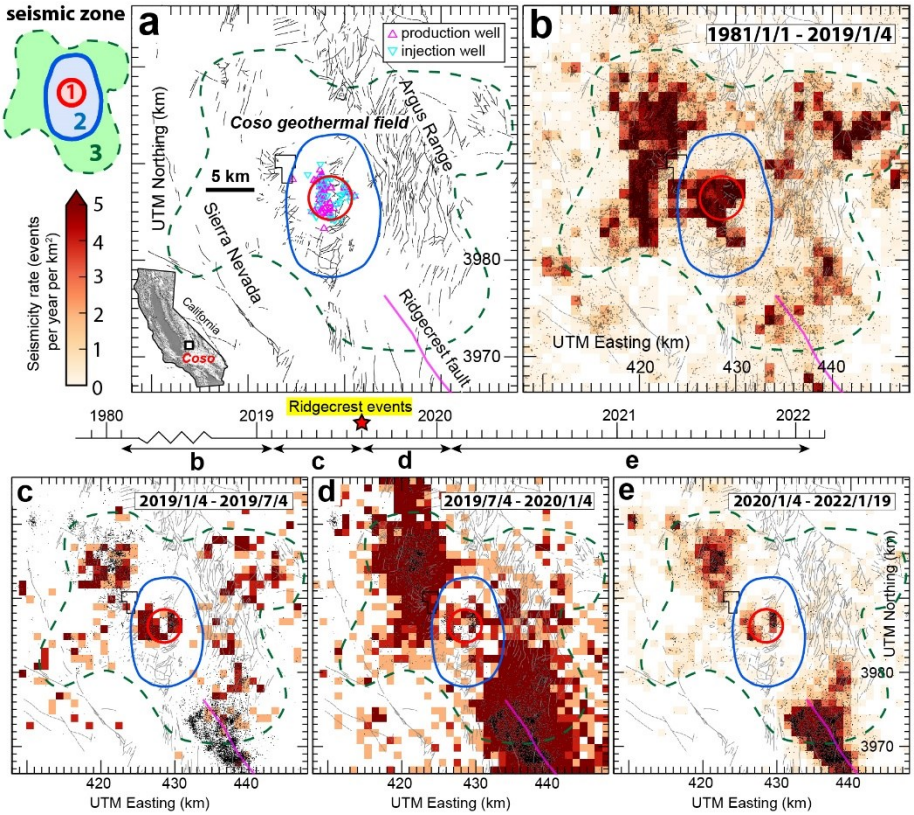

Figure 2. (a) The Coso geothermal field is divided into three distinct seismic zones. Epicenters from the SCEC community catalog are depicted as brown dots. Seismic activity density is shown as events per year per square kilometer, with a minimum magnitude of -1.02. (Hauksson et al., 2012) during (b) 1981/1/1 – 2019/1/4, (c) 2019/1/4-2019/7/4, (d) 2019/7/4 – 2020/1/4 and (e) 2020/1/4 – 2022/1/19. Please note that Zone 1's seismicity is not included in Zone 2 or Zone 3. Likewise, Zone 2's seismicity is not included in Zone 3 (after Tung et al., 2024).

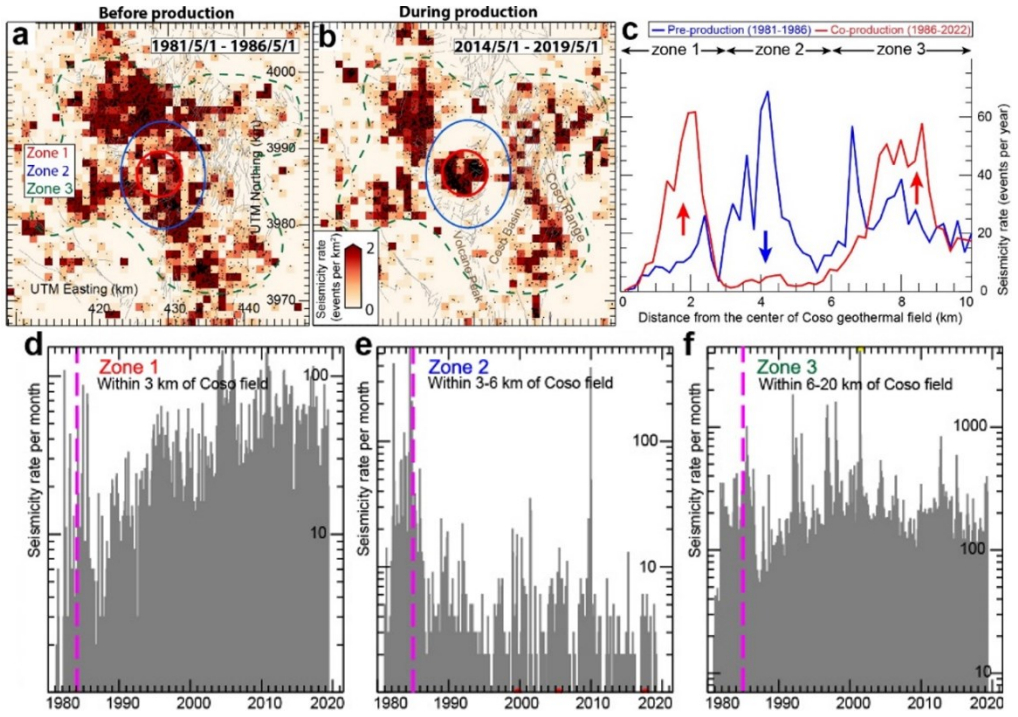

Figure 3. Seismicity distributions (a) before and (b) after the onset (i.e., May 1986) of geothermal energy production at Coso. The three seismic zones exhibit different (c) seismicity rates before (blue line) and during (red line) geothermal production (after Tung et al., 2024). The evolving seismicity rates of Zone 1, 2, and 3 are plotted in (d), (e), and (f) respectively.

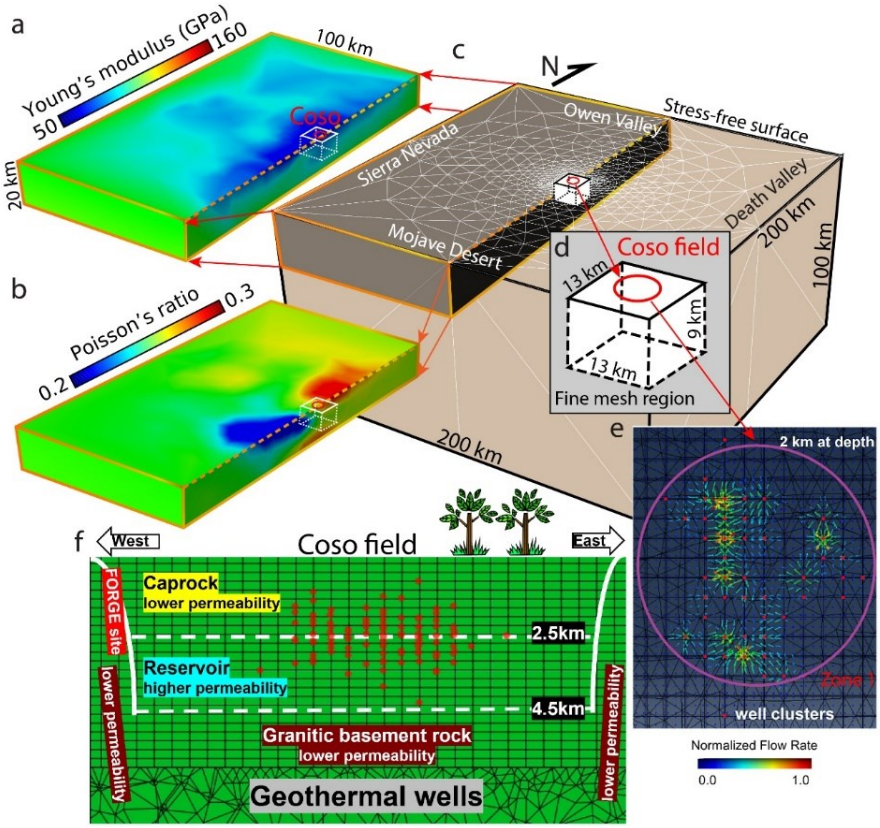

Figure 4. Finite Element Model for Elastic and Poroelastic Simulation. (a) The spatial variation in Young's modulus defines rock heterogeneity. (b) The spatial variation in Poisson's ratio also contributes to rock heterogeneity within (c) the numerical domain, which simulates the greater Coso region. (d) A fine-mesh region is created near the top center to accommodate the injection and production wells. (e) A flow vector map at 2 km depth during the injection/production operation through wells, shown as red dots. (f) A simplified 3D permeability distribution hydrological model (refer to Table 1) is incorporated into the poroelastic domain to simulate surface-subsurface fluid exchange through geothermal wells, indicated by red dots (after Tung et al., 2024).

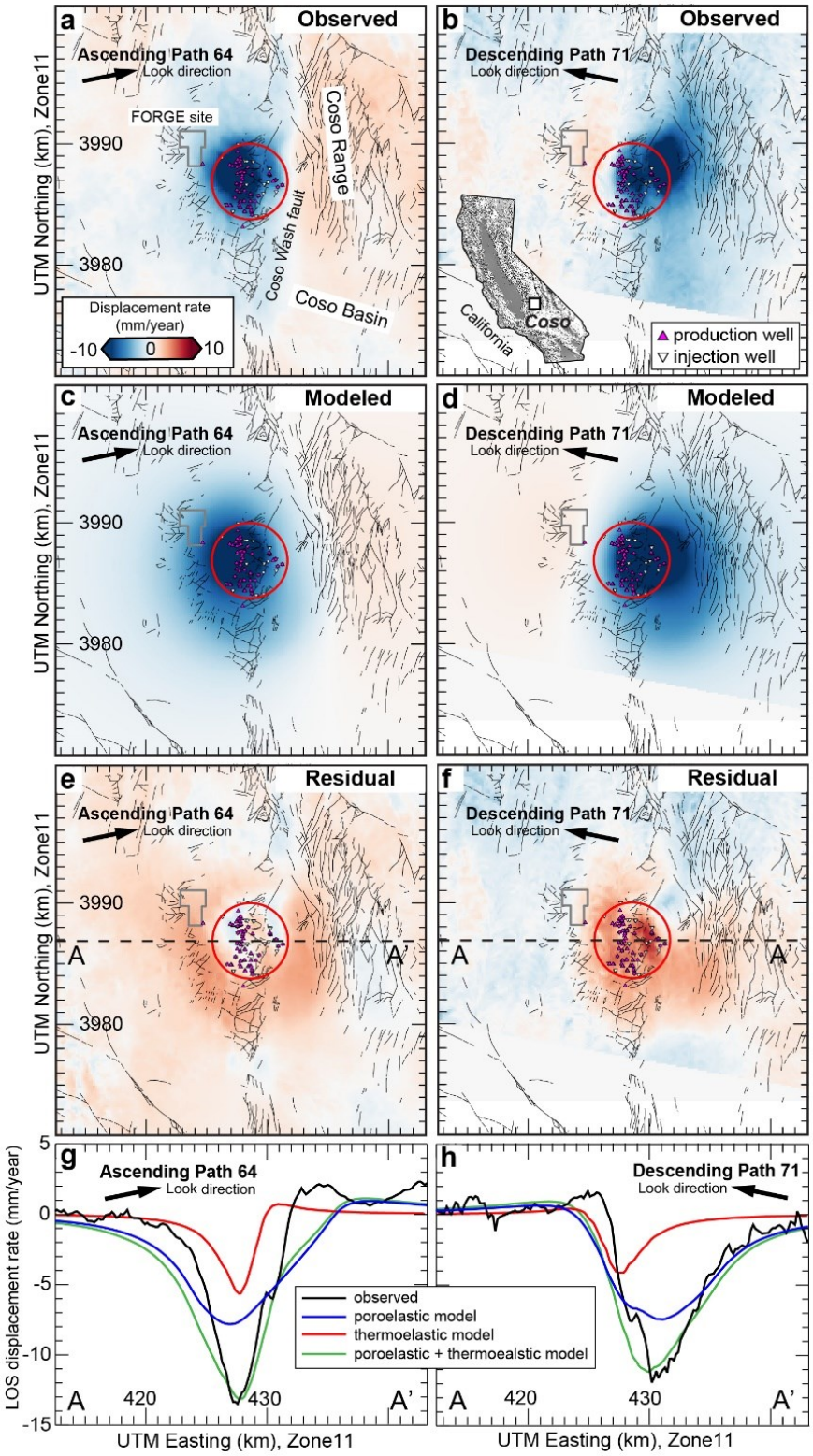

Figure 5. LOS ground displacement rate at the Coso field from 2014 to 2019 (Period (1)) before the 2019 July 4 Ridgecrest earthquake. (a, b) show the observed displacement rates along the ascending and descending paths 64 and 71, respectively. (c, d) depict the modeled displacement rates, combining poroelastic and thermoelastic effects, along the same paths. (e, f) illustrate the residual displacement rates. A subsidence rate of up to 15 ± 0.4 mm/year is recorded over the main flank. (g, h) present the observed and modeled displacement profiles along the cross-section AA' through the center of the Coso geothermal field. The Coso nearfield and proposed FORGE site are marked in red and grey, respectively. The residuals have an average value of less than 1 mm/year, with the mean-residual-to-max-displacement ratio ranging from 6.6% to 7.7% (after Tung et al., 2024).

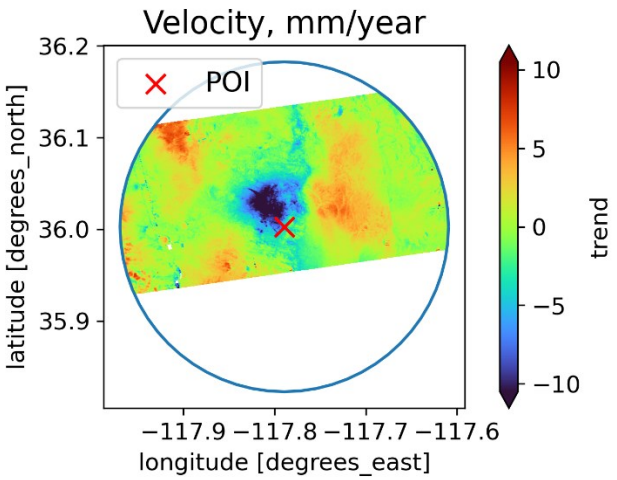

Figure 6. LOS ground displacement rate at the Coso field between 2020 – 2022 (Period (2)) after the 2019 July 4 Ridgecrest earthquake. The Coso geothermal power plant is denoted by the red cross.

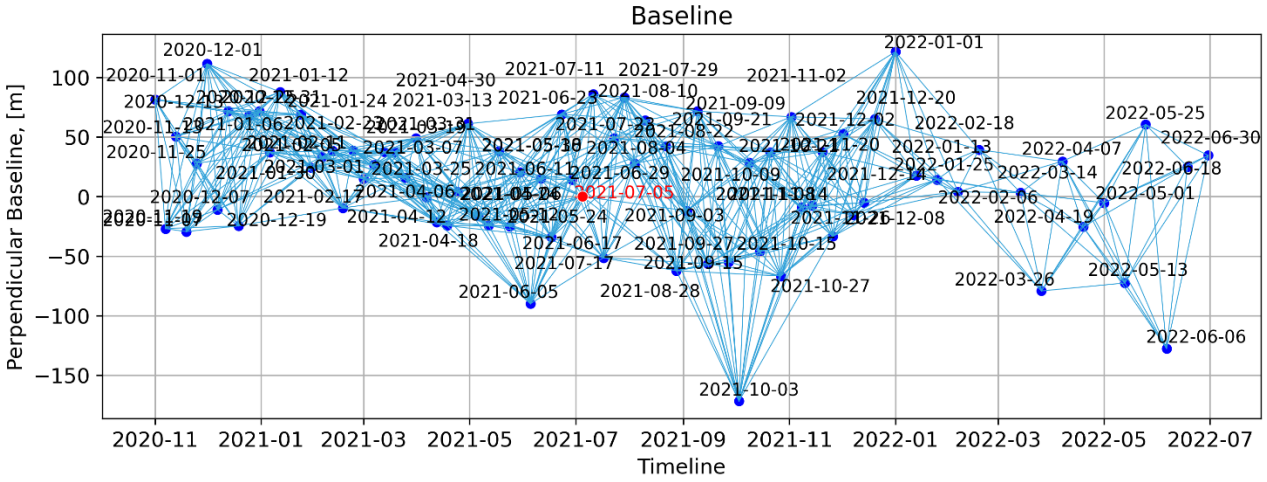

Figure 7. Temporal and perpendicular baseline network of the InSAR pairs between 2020 – 2022 (Period (2)) after the 2019 July 4 Ridgecrest earthquake.

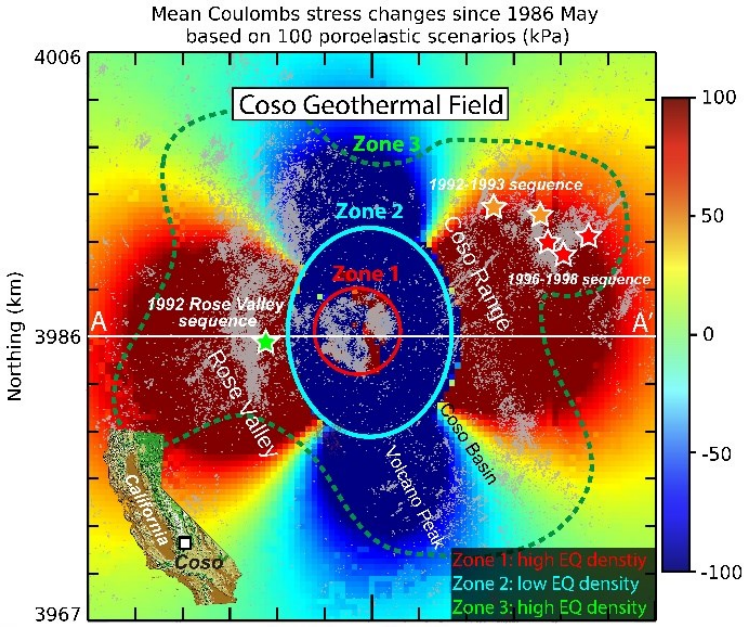

Figure 8. Average Coulomb stress variations from 1986 to 2021, based on 100 poroelastic scenario simulations. Grey dots represent the seismic events recorded during this timeframe (after Tung et al., 2024).

Layer ID	Depth (km)	$\log_{10}(k)$ (m^2)	Φ (%)	α	Θ (%)	Description	References
1	0-2.5	-16	5	0.7	100	Clay-rich caprock	(Davatzes and Hickman, 2010; Im et al., 2021; Lees, 2002; Rose, 2013; Siler et al., 2016; Wamalwa et al., 2013; Wang, 2000)
2	2.5-4.5	-13	10	0.5	100	Geothermal reservoir	(Davatzes and Hickman, 2010; Im et al., 2021; Monastero et al., 2005; Rose, 2013; Sabin et al., 2016; Siler et al., 2016; Wang, 2000)
3	4.5-6	-16	5	0.5	100	Basement rock	(Davatzes and Hickman, 2010; Hauksson and Unruh, 2007; Im et al., 2021; Siler et al., 2016; Wang et al., 2022; Wang, 2000)
Outside Coso	0-15	-17	5	0.5	100	Country rock	(Davatzes and Hickman, 2010; Im et al., 2021; Siler et al., 2016; Wang et al., 2022; Wang, 2000; Zhang and Lin, 2014)

Table 1. Simplified layered structure and its surroundings of the Coso field (c.f. Figure 4f), given intrinsic rock permeability, k, porosity, φ, and the degree of saturation, θ (after Tung et al., 2024).

ACKNOWLEDGMENTS

The authors extend their gratitude to Ole Kaven, Kelly Blake and Andrew Sabin for their invaluable knowledge exchange related to the Coso geothermal field. Sui Tung and Kurt Feigl's work was funded by the WHOLESCALE project (DE-EE0009032). Additionally, Sui Tung and Manoochehr Shirzaei received partial funding from a U.S. Department of Energy grant (SC0019307). Sui Tung's research also benefited from NSF award #2326785, NSF sub-award #S001463, and SCEC award #24192. The authors are also grateful to the European Space Agency (ESA) for providing the Sentinel-1 Synthetic Aperture Radar data and to the Southern California Earthquake Center (SCEC) for the relocated seismic catalog of southern California.

REFERENCES

Barbour, A. J., Evans, E. L., Hickman, S. H., and Eneva, M., 2016, Subsidence rates at the southern Salton Sea consistent with reservoir depletion: Journal of Geophysical Research: Solid Earth, v. 121, no. 7, p. 5308-5327.

Barbour, A. J., Norbeck, J. H., and Rubinstein, J. L., 2017, The effects of varying injection rates in Osage County, Oklahoma, on the 2016 M w 5.8 Pawnee earthquake: Seismological Research Letters, v. 88, no. 4, p. 1040-1053.

Bassin, C., Laske, G., and Masters, G., 2000, The current limits of resolution for surface wave tomography in {North America}: Eos, v. 81.

CDC, 2022, Geothermal Production and Injection Data Maps from California Department of Conservation.

Davatzes, N. C., and Hickman, S. H., The feedback between stress, faulting, and fluid flow: Lessons from the Coso Geothermal Field, CA, USA, *in* Proceedings Proceedings World Geothermal Congress 20102010, p. 1-14.

Eneva, M., Barbour, A., Adams, D., Hsiao, V., Blake, K., Falorni, G., and Locatelli, R., 2018, Satellite observations of surface deformation at the Coso geothermal field, California: GRC Trans, v. 42, p. 1383-1401.

Goebel, T., Weingarten, M., Chen, X., Haffener, J., and Brodsky, E., 2017, The 2016 Mw5. 1 Fairview, Oklahoma earthquakes: Evidence for long-range poroelastic triggering at> 40 km from fluid disposal wells: Earth and Planetary Science Letters, v. 472, p. 50-61.

Goebel, T. H. W., and Brodsky, E. E., 2018, The spatial footprint of injection wells in a global compilation of induced earthquake sequences: Science, v. 361, no. 6405, p. 899-904.

Hauksson, E., and Unruh, J., 2007, Regional tectonics of the Coso geothermal area along the intracontinental plate boundary in central eastern California: Three-dimensional Vp and Vp/Vs models, spatial-temporal seismicity patterns, and seismogenic deformation: Journal of Geophysical Research: Solid Earth (1978–2012), v. 112, no. B6.

Hauksson, E., Yang, W., and Shearer, P. M., 2012, Waveform Relocated Earthquake Catalog for Southern California (1981 to June 2011): Bulletin of the Seismological Society of America, v. 102, no. 5, p. 2239-2244.

Hauksson, E., Yoon, C., Yu, E., Andrews, J. R., Alvarez, M., Bhadha, R., and Thomas, V., 2020, Caltech/USGS Southern California Seismic Network (SCSN) and Southern California Earthquake Data Center (SCEDC): Data Availability for the 2019 Ridgecrest Sequence: Seismological Research Letters, v. 91, no. 4, p. 1961-1970.

Im, K., Avouac, J. P., Heimisson, E. R., and Elsworth, D., 2021, Ridgecrest aftershocks at Coso suppressed by thermal destressing: Nature, v. 595, no. 7865, p. 70-74.

Lees, J. M., 2002, Three-dimensional anatomy of a geothermal field, Coso, southeast-central California: Geologic Evolution of the Mojave Desert and Southwestern Basin and Range, Boulder, Colorado, Geological Society of America Memoirs, v. 195, p. 259-276.

Li, B. Q., Khoshmanesh, M., and Avouac, J. P., 2021, Surface Deformation and Seismicity Induced by Poroelastic Stress at the Raft River Geothermal Field, Idaho, USA: Geophysical Research Letters, v. 48, no. 18.

Monastero, F. C., Katzenstein, A. M., Miller, J. S., Unruh, J. R., Adams, M. C., and Richards-Dinger, K., 2005, The Coso geothermal field: A nascent metamorphic core complex: Geological Society of America Bulletin, v. 117, no. 11.

Plesch, A., Tape, C., Shaw, J. H., Small, P., Ely, G., and Jordan, T., 2011, User Guide for the Southern California Earthquake Center Community Velocity Model: SCEC CVM-H 11.9.0.

Rose, P. E., 2013, Creation of an enhanced geothermal system through hydraulic and thermal stimulation: Energy and Geoscience Institute at the University of Utah.

Sabin, A., Blake, K., Lazaro, M., Meade, D., Blankenship, D., Kennedy, M., McCulloch, J., DeOreo, S., Hickman, S., and Glen, J., Geologic setting of the West Flank, a FORGE site adjacent to the Coso geothermal field, *in* Proceedings 41st Workshop on Geothermal Reservoir Engineering, Stanford University, Stanford, CA2016.

Siler, D. L., Blake, K., Sabin, A., Lazaro, M., Meade, D., Blankenship, D., Kennedy, B. M., McCulloch, J., DeOreo, S., and Hickman, S., 2016, The geologic framework of the West Flank FORGE site: GRC Transactions, v. 40, p. 585-595.

Tung, S., Kaven, O., Shirzaei, M., Masterlark, T., Wang, H. F., Huang, W.-C., and Feigl, K. L., 2024, Seismicity zoning at Coso geothermal field and stress changes from fluid production and migration: Earth and Planetary Science Letters, v. 646, p. 119000.

Tung, S., and Masterlark, T., 2018, Delayed poroelastic triggering of the 2016 October Visso earthquake by the August Amatrice earthquake, Italy: Geophysical Research Letters, v. 45, no. 5, p. 2221-2229.

Tung, S., Masterlark, T., and Dovovan, T., 2018, Transient poroelastic stress coupling between the 2015 M7.8 Gorkha, Nepal earthquake and its M7.3 aftershock: Tectonophysics, v. 733, p. 119-131.

Tung, S., Zhai, G., and Shirzaei, M., 2021, Potential Link Between 2020 Mentone, West Texas M5 Earthquake and Nearby Wastewater Injection: Implications for Aquifer Mechanical Properties: Geophysical Research Letters, v. 48, no. 3.

Wamalwa, A. M., Mickus, K. L., Serpa, L. F., and Doser, D. I., 2013, A joint geophysical analysis of the Coso geothermal field, south-eastern California: Physics of the Earth and Planetary Interiors, v. 214, p. 25-34.

Wang, D., Wu, S., Li, T., Tong, P., and Gao, Y., 2022, Elongated Magma Plumbing System Beneath the Coso Volcanic Field, California, Constrained by Seismic Reflection Tomography: Journal of Geophysical Research: Solid Earth, v. 127, no. 6.

Wang, H., 2000, Theory of Linear Poroelasticity: With Applications to Geomechanics and Hydrogeology, Princeton University Press.

Zhang, and Lin, G., 2014, Three-dimensional Vp and Vp/Vs models in the Coso geothermal area, California: Seismic characterization of the magmatic system: Journal of Geophysical Research: Solid Earth, v. 119, no. 6, p. 4907-4922.

Zhang, Q., Lin, G., Zhan, Z., Chen, X., Qin, Y., and Wdowinski, S., 2017, Absence of remote earthquake triggering within the Coso and Salton Sea geothermal production fields: Geophysical Research Letters, v. 44, no. 2, p. 726-733.